Published in final edited form as:
J Nucl Med. 2010 August ; 51(8): 1293–1300. doi:10.2967/jnumed.110.076174.

^{89}Zr-DFO-J591 for immunoPET imaging of prostate-specific membrane antigen (PSMA) expression *in vivo*

Jason P. Holland[a], **Vadim Divilov**[a], **Neil H. Bander**[b], **Peter M. Smith-Jones**[a,c], **Steven M. Larson**[c,d,e], and **Jason S. Lewis**[a,e,*]

[a]Radiochemistry Service, Department of Radiology, Memorial Sloan-Kettering Cancer Center, 1275 York Avenue, New York, United States of America, NY10065

[b]Laboratory of Urological Oncology, Department of Urology, New York-Presbyterian Hospital, Weill Medical College of Cornell University, 525 E. 68th Street, and Department of Urology, Memorial Sloan-Kettering Cancer Center, New York, United States of America, NY10065

[c]Ludwig Center for Cancer Immunotherapy, Sloan-Kettering Institute, Memorial Sloan-Kettering Cancer Center, 1275 York Avenue, New York, United States of America, NY10065

[d]Nuclear Medicine Service, Department of Radiology, Memorial Sloan-Kettering Cancer Center, 1275 York Avenue, New York, United States of America, NY10065

[e]Program in Molecular Pharmacology and Chemistry, Memorial Sloan-Kettering Cancer Center, 1275 York Avenue, New York, United States of America, NY10065

Abstract

Zirconium-89 ($t_{1/2}$ = 3.27 days) is a positron emitting radionuclide which displays excellent potential for use in the design and synthesis of radioimmunoconjugates for immunoPET. In these studies we report the preparation of ^{89}Zr-DFO-J591, a novel ^{89}Zr -labeled monoclonal antibody (mAb) construct for targeted immunoPET imaging and quantification of prostate-specific membrane antigen (PSMA) expression *in vivo*.

Methods—The *in vivo* behavior of [^{89}Zr]Zr-chloride, [^{89}Zr]Zr-oxalate and [^{89}Zr]Zr-DFO was investigated by using PET imaging. High level computational studies using density functional theory (DFT) calculations have been used to investigate the electronic structure of [^{89}Zr]Zr-DFO and probe the nature of the complex in aqueous conditions. J591 was functionalized with the hexadentate, *tris*-hydroxamate ligand desferrioxamine B (DFO) and radiolabeled with [^{89}Zr]Zr-oxalate at room temperature. ImmunoPET imaging experiments in male, athymic *nu*/*nu* mice bearing sub-cutaneous LNCaP (PSMA positive) or PC-3 (PSMA negative) tumors were conducted. The change in ^{89}Zr-DFO-J591 tissue uptake in response to high- and low-specific-activity formulations in the two tumor models was measured by using acute biodistribution studies and immunoPET.

Results—Basic characterization of three important reagents, [^{89}Zr]Zr-chloride and [^{89}Zr]Zr-oxalate, as well as the complex, [^{89}Zr]Zr-DFO, demonstrated that the nature of the ^{89}Zr species

[*]**Corresponding Author:** Jason S. Lewis, Ph.D., Radiochemistry Service, Department of Radiology, Memorial Sloan-Kettering Cancer Center, 1275 York Avenue, New York, New York 10065, Tel: (646)-888-3038, Fax: (646)-422-0408, lewisj2@mskcc.org.
First Author: Jason P. Holland, D.Phil, Post-Doctoral Research Scholar, Radiochemistry Service, Department of Radiology, Memorial Sloan-Kettering Cancer Center, 1275 York Avenue, New York, New York 10065, Tel: (646)-888-3083, Fax: (646)-422-0408, hollanj3@mskcc.org

Disclosures: Dr. Bander is the inventor on patents that are owned by Cornell Research Foundation ("CRF") for the J591 antibody described in this manuscript. Dr. Bander is a paid consultant to BZL Biologics, the company to which the patents were licensed by CRF for further research and development.

has a dramatic effect on the biodistribution and pharmacokinetics. DFT calculations provide a rationale for the observed high *in vivo* stability of ^{89}Zr-DFO-labeled mAbs and suggest that in aqueous conditions, [^{89}Zr]Zr-DFO forms a thermodynamically stable, 8-coordinate complex by coordination of two water molecules. ^{89}Zr-DFO-J591 was produced in high radiochemical yield (>77%) with radiochemical purity >99% and a specific-activity of 181.7±1.1 MBq/mg (4.91±0.03 mCi/mg). *In vitro* assays demonstrated that ^{89}Zr-DFO-J591 had an initial immunoreactive fraction of 0.95±0.03 and remains active for up to 7 days. *In vivo* biodistribution experiments revealed high uptake of ^{89}Zr-DFO-J591 in LNCaP tumors after 24, 48, 96 and 144 h (34.4±3.2 %ID/g; 38.0±6.2 %ID/g; 40.4±4.8 %ID/g; and 45.8±3.2 %ID/g, respectively). Specificity for PSMA expression was confirmed by biodistribution studies in PC-3 (PSMA negative) tumor models and by using low specific activity competitive inhibition studies. ImmunoPET studies also demonstrated that ^{89}Zr-DFO-J591 provides excellent image contrast with tumor-to-muscle ratios >20 for delineation of LNCaP tumors between 48 – 144 h post-administration.

Conclusion—These experimental and computational studies demonstrate that ^{89}Zr-DFO-labeled mAbs show exceptional promise as radiotracers for immunoPET imaging of human cancers. ^{89}Zr-DFO-J591 displays tumor-to-background tissue contrast in immunoPET and can be used to delineate and quantify PSMA-positive prostate tumors *in vivo*.

Keywords

ImmunoPET; zirconium-89; prostate-specific membrane antigen (PSMA); J591; monoclonal antibodies; density functional theory

Introduction

The National Cancer Institute (NCI) estimates that in the United States during 2009, approximately 192,000 cases of prostate cancer (PC) will have been diagnosed with a projected mortality rate of over 27,000 men (>14%). Despite the high incidence of PC, standard diagnostic imaging techniques used for the detection and monitoring of therapy remain inadequate. For example, early stage, hormonally sensitive tumors on treatment, and non-castrate PCs often appear negative in positron emission tomography (PET) scans using either the metabolic radiotracer, [^{18}F]-FDG or the hormone-based radiopharmaceutical, 16β-[^{18}F]-dihydrotestosterone ([^{18}F]-FDHT) for imaging overexpression of androgen receptors. (1) Therefore, there is an urgent requirement to develop new tools for non-invasive delineation and staging of PC *in vivo*.

Prostate-specific membrane antigen (PSMA) is a 100 kDa, type II transmembrane glycoprotein and is one of the best characterized oncogenic markers/targets.(2,3) PSMA expression has been detected in a limited range of normal tissues including benign prostatic epithelium, renal proximal tubule, small bowel and brain (a subset of astrocytes). However, these normal sites express PSMA at levels 2–3 orders of magnitude lower than that observed in more than 95% of clinical PC specimens.(4,5) In addition, as these normal tissue PSMA sites are highly polarized to the apical/luminal aspect of the benign prostatic glands, renal tubules and small bowel, basement membrane and epithelial tight junctions they form substantial barriers to circulating mAbs. PSMA expression by astrocytes is similarly sequestered behind the blood-brain barrier. As a result, antibodies to PSMA are functionally tumor-specific, whereas small molecule PSMA ligands excreted *via* the renal tubular lumen are not.

PSMA expression levels have been shown exhibit a positive correlation with increased tumor aggression, metastatic spread and the development of castrate-resistance or resistance to hormone-based therapies. PSMA expression has also been reported in the neovasculature

of most solid tumors.(6) The failure of [^{18}F]-FDG-PET for detecting early and treated PC, and the acquired resistance of many advanced PCs to androgen-based agents has been the driving force behind recent efforts towards developing novel chemo- and radioimmunoconjugate based drugs and imaging agents. In particular, in 1996 the United States Food and Drug Administration (US-FDA) approved the use of [^{111}In]-ProstaScint ([^{111}In]-Capromab pendetide or [^{111}In]-7E11), a murine-mAb specific for an *intracellular* epitope of PSMA, for single-photon emission computed tomography (SPECT) imaging of PC soft tissue metastases. However, [^{111}In]-ProstaScint for clinical diagnosis is sub-optimal because of low sensitivity for viable tumor sites (62% for lymph node metastases; 50% for prostate bed recurrence) which is probably because the number of available targets (presented in dead/dying tissue) is limited. Furthermore, [^{111}In]-ProstaScint does not bind to viable PC sites in bone (the most common site of metastatic disease), and in contrast to PET, SPECT imaging remains only semi-quantitative in the clinical setting. Despite these limitations, [^{111}In]-ProstaScint has its supporters, and is still recommended as being useful for specific clinical situations by the National Comprehensive Cancer Network (NCCN) Clinical Practice Guidelines.(5) The NCCN recommends the use of [^{111}In]-ProstaScint before salvage therapy after radiotherapy or prostatectomy. This fact is testament to the relative lack of better imaging methods for detection of metastatic prostate cancer, especially in soft-tissue.

In 1997, Liu *et al*. produced 4 mAbs (IgG_1: J415, J533 and J591; and IgG_3: E99) specific for binding to two distinct epitopes ($PSMA_{ext1}$ and $PSMA_{ext2}$) on the extracellular domain of PSMA.(7,8) Subsequent *in vitro* and *in vivo* studies by Smith-Jones *et al*.(9,10) and McDevitt *et al*.(11) identified J591 as the most promising candidate for developing diagnostic and therapeutic immunoconjugates targeting extracellular PSMA in viable tissue. Since these initial studies, J591 has been humanized and a range of preclinical and clinical studies using J591 radiolabeled with ^{90}Y, ^{177}Lu or ^{131}I for β-therapy, ^{213}Bi and ^{225}Ac for α-therapy, and ^{111}In for SPECT imaging have been reported.(9–20)

Positron Emission Tomography has advantages over SPECT imaging in terms of sensitivity and contrast resolution, especially for tissues at a depth within the body, and these improved imaging characteristics are particularly important for radioimmuno-imaging. The work presented here describes the production and preclinical evaluation of ^{89}Zr-radiolabeled J591 for targeted immunoPET imaging of PSMA-positive tumors *in vivo*. The new radiopharmaceutical, ^{89}Zr-DFO-J591, has been characterized by a range of stability and cellular association assays *in vitro*. The nature of the electronic structure of [^{89}Zr]Zr-DFO complex has been explored by using high level density functional theory (DFT) calculations and the computational results provide a rationale for the high experimentally observed *in vitro* and *in vivo* stability of the [^{89}Zr]Zr-DFO-labeled radioimmunoconjugates. The ability of ^{89}Zr-DFO-J591 to target PSMA expressing tissue has also been examined by using acute biodistribution studies and immunoPET imaging *in vivo*. The results demonstrate that ^{89}Zr-DFO-J591 has potential to be used in the clinic as a radiotracer for both improved localization and staging of PSMA-positive tumors.

Materials and Methods

All chemicals, unless otherwise stated, were purchase from SigmaAldrich (St. Louis, MO) and were used as received. Water (>18.2 MΩ·cm at 25 °C, Milli-Q, Millipore, Billerica, MA) was purified by passing through a 10 cm column of chelex resin (Bio-Rad Laboratories, Hercules, CA) at a flow rate <1.0 mL/min. All instruments were calibrated and maintained in accordance with previously reported routine quality-control procedures.(21) Radioactivity measurements were made by using a Capintec CRC-15R Dose Calibrator (Capintec, Ramsey, NJ) with a calibration factor of 465 for ^{89}Zr. For accurate quantification

of radioactivities, experimental samples were counted for 1 min. on a calibrated Perkin Elmer (Waltham, MA) Automatic Wizard^2 Gamma Counter by using a dynamic energy window of 800–1000 keV for ^{89}Zr (909 keV emission). ^{89}Zr-radiolabeling reactions were monitored by using silica-gel impregnated glass-fibre instant thin-layer chromatography (ITLC-SG) paper (Pall Corp., East Hills, NY) and analyzed on a radio-TLC plate reader (Bioscan System 200 Imaging Scanner coupled to a Bioscan Autochanger 1000 (Bioscan Inc., Washington, DC, using Win-Scan Radio-TLC software version 2.2). Solvent systems included diethylene triamine pentaacetic acid in water (DTPA, 50 mM, pH7) and phosphate buffered saline (PBS). Human prostate cancer cell lines LNCaP and PC-3 were obtained from the American Type Culture Collection (ATCC, Manassas, VA) and were grown by serial passage.

Density functional theory calculations

All calculations were conducted using density functional theory (DFT) as implemented in the Gaussian03 suite of *ab initio* quantum chemistry programs.(22) Full computational details and Cartesian coordinates of the optimized structures are presented in the **supporting information**. Energetic values are reported in S.I. units of kJ mol^{-1}.

Antibody conjugation and radiolabeling

The IgG$_1$ monoclonal antibody J591 was conjugated to the *tris*-hydroxamate, hexadentate chelate, desferrioxamine B (DFO, Calbiochem, Spring Valley, CA) by using a 6-step procedure modified from that described by Verel *et al*.(23) Full details are provided in the supporting information.

Zirconium-89 was produced *via* the ^{89}Y(*p*,*n*)^{89}Zr transmutation reaction on an EBCO TR19/9 variable beam energy cyclotron (Ebco Industries Inc., Richmond, British Columbia, Canada) in accordance with previously reported methods.(23,24) The [^{89}Zr]Zr-oxalate was isolated in high radionuclidic and radiochemical purity (RCP) >99.9%, with an effective specific-activity of 195–497 MBq/μg, (5.28–13.43 mCi/μg).(24)

^{89}Zr-DFO-J591 was prepared by the complexation of [^{89}Zr]Zr-oxalate with DFO-J591. Typical radiolabeling reactions were conducted in accordance with the following procedure. Briefly, [^{89}Zr]Zr-oxalate (153.2 MBq, [4.14 mCi]) in 1.0 M oxalic acid (170 μL) was adjusted to pH7.7–8.1 with 1.0 M Na_2CO_3(aq.). CAUTION: Acid neutralization releases CO_2(g) and care should be taken to ensure that no radioactivity escapes the microcentrifuge vial. After CO_2(g) evolution ceased, DFO-J591 (400 μL, 2.1 mg/mL [0.84 mg of mAb], in 0.9% sterile saline) was added and the reaction was mixed gently by aspirating with a pipette. The reaction was incubated at room temperature for between 1–2 h and complexation progress was monitored with respect to time by ITLC (DTPA, 50 mM, pH7). After 1 h, crude radiolabeling yields and RCP was >95%. ^{89}Zr-DFO-J591 was purified by using either size-exclusion chromatography (Sephadex G-25 M, PD-10 column, >30 kDa, GE Healthcare; dead-volume = 2.5 mL, eluted with 200 μL fractions of 0.9% sterile saline) or spin-column centrifugation (4 mL total volume, >30 kDa, Amicon Ultra-4, Millipore, Billerica, MA; washed with 4×3 mL, 0.9% sterile saline). The radiochemical purity (RCP) of the final ^{89}Zr-DFO-J591 (>77% radiochemical yield; formulation: pH5.5–6.0; <500 μL; 0.9% sterile saline) was measured by both radio-ITLC and analytical size-exclusion chromatography (loading <0.74 MBq [20 μCi], ca. 5–10 μL aliquots) and was found to be >99% in all preparations. In the ITLC experiment ^{89}Zr-DFO-J591 and [^{89}Zr]Zr-DFO remain at the baseline (R_f = 0.0), whereas $^{89}Zr^{4+}$(aq.) ions and [^{89}Zr]Zr-DTPA elute with the solvent front (R_f = 1.0).

Chelate number

The number of accessible DFO chelates conjugated to J591 was measured by radiometric isotopic dilution assays following a method similar to that described by Anderson *et al*.(25) From a stock solution, aliquots of [^{89}Zr]Zr-oxalate (10 μL, 660 kBq [18 μCi], pH7.7–8.1 [pH adjusted using 1.0 M Na_2CO_3]) were added to 10 solutions containing 1:2 serial dilutions of non-radioactive $ZrCl_4$(aq.) (50 μL fractions; 250–0.5 pmol, pH7.7–8.1). The mixture was vortexed for 30 s before adding aliquots of DFO-J591 (5 μL, 2.1 mg/mL, [10.5 μg of mAb, 0.07 nmol], in 0.9% saline). The reactions were incubated at room temperature for 2 h before quenching with DTPA (20 μL, 50 mM, pH7). Control experiments confirmed that ^{89}Zr complexation to DFO-J591 was complete within <2 h. The extent of complexation was assessed by developing ITLC strips (DTPA, 50 mM) and counting the activity at the baseline and solvent front. The fraction of ^{89}Zr-radiolabeled mAb (A_b) was plotted *versus* the amount of non-radioactive $ZrCl_4$ added. The number of chelates was calculated by using linear regression analysis to calculate the concentration of $ZrCl_4$ at which only 50% of the DFO-J591 was labeled, multiplying by a factor of 2, and then dividing by the moles of mAb present in the reaction.

Immunoreactivity

The immunoreactive fraction of ^{89}Zr-DFO-J591 was determined by using specific radioactive cellular-binding assays following modified procedures derived from Lindmo *et al*.(26) Briefly, LNCaP or PC-3 cells were suspended in micro-centrifuge tubes at concentrations of 5.0, 4.0, 3.0, 2.5, 2.0, 1.5, and 0.5 $\times 10^6$ cells/mL in 500 μL PBS (pH7.4). Aliquots (50 μL, <0.37 kBq, [<0.01 μCi]) of ^{89}Zr-DFO-J591 in 1% bovine serum albumin (BSA) were added to each tube (n = 3; final volume: 550 μL) and the samples were incubated on an orbital mixer for 60 min. at room temperature. Cells were then pelleted by centrifugation (600G for 2 min.), resuspended and washed twice with ice-cold PBS before removing the supernatant and counting the ^{89}Zr-radioactivity associated with the cell pellet. The count data were background corrected and compared with the total number of counts in control samples. Non-specific binding was assessed by using the same methods but with PC-3 (PSMA-negative) cells in place of LNCaP cells. Immunoreactive fractions were determined by linear regression analysis of a plot of (total/bound) activity *versus* (1/[normalized number of cells]), and calculated as 1/y-intercept.

Stability studies

The stability of ^{89}Zr-DFO-J591 with respect to change in radiochemical purity, loss of radioactivity from the mAb and/or change in immunoreactivity was investigated *in vitro* by incubation in solutions of 0.9% saline, and 1% BSA for 7 days at 37°C. The radiochemical purity was determined by radio-ITLC and γ-counting, and the immunoreactive fraction was measured by using the LNCaP cellular-binding assay (*vide supra*).

Xenograft models

All animal experiments were conducted in compliance with Institutional Animal Care and Use Committee (IACUC) guidelines. Male athymic *nu/nu* mice (NCRNU-M, 20–22 g, 6–8 weeks old) were obtained from Taconic Farms Inc. (Hudson, NY), and were allowed to acclimatize at the MSKCC vivarium for 1 week prior to implanting tumors. Mice were provided with food and water *ad libitum*. LNCaP tumors were induced on the left shoulder by sub-cutaneous (s.c.) injection of 4.0×10^6 cells in a 200 μL cell suspension of a 1:1 v/v mixture of media with reconstituted basement membrane (BD Matrigel™, Collaborative Biomedical Products Inc., Bedford, MA). Similarly, PC-3 tumors were induced on the right shoulder by s.c. injection of 5.0×10^6 cells. Palpable LNCaP tumors (50–250 mm^3) developed after a period of 24–30 days. PC-3 tumors (70–90 mm^3) grew more rapidly with

more uniform size distribution and were suitable for use for *in vivo* studies after 10–14 days. The tumor volume (V / mm^3) was estimated by external vernier caliper measurements of the longest axis, a / mm, and the axis perpendicular to the longest axis, b / mm. The tumors were assumed to be spheroidal and the volume was calculated in accordance with Equation 1.(27)

$$V=\frac{4\pi}{3}\cdot\left(\frac{a}{2}\right)^2\cdot\frac{b}{2} \quad (1)$$

Acute biodistribution studies

Acute *in vivo* biodistribution studies were conducted to evaluate the uptake of ^{89}Zr-DFO-J591 in mice bearing s.c. LNCaP (50–250 mm^3) or PC-3 (70–90 mm^3) tumors. Mice were randomized before the study and were warmed gently with a heat lamp 5 min. before administering ^{89}Zr-DFO-J591 (0.55–0.74 MBq, [15–20 μCi], 3–4 μg of mAb, in 200 μL 0.9% sterile saline for injection) *via* intravenous (i.v.) tail-vein injection (t=0 h). Animals (n = 3–5, per group) were euthanized by CO_2(g) asphyxiation at 24, 48, 96 and 144 h post-injection and 12 organs (including the tumor) were removed, rinsed in water, dried in air for 5 min., weighed and counted on a gamma-counter for accumulation of ^{89}Zr-radioactivity. The mass of ^{89}Zr-DFO-J591 formulation injected into each animal was measured and used to determine the total number of counts (counts per minute, [c.p.m.]) by comparison to a standard syringe of known activity and mass. Count data were background- and decay-corrected and the percentage injected dose per gram (%ID/g) for each tissue sample was calculated by normalization to the total amount of activity injected.

Competitive inhibition studies were also performed *in vivo* to investigate the specificity of ^{89}Zr-DFO-J591 for PSMA. Non-radiolabeled J591 (5 mg/kg solution in 0.9% sterile saline, 0.3 mg/mouse) was added to the ^{89}Zr-DFO-J591 formulation to reduce the specific-activity (60-fold decrease: 3.04 MBq/mg [0.082 mCi/mg]) and biodistribution studies were performed at 48 h post-i.v. administration (n=4).

Small-animal immunoPET imaging

PET imaging experiments were conducted on a microPET Focus 120 scanner (Concorde Microsystems).(28) Mice were administered ^{89}Zr-DFO-J591 formulations (10.9–11.3 MBq, [295–305 μCi], 60–62 μg of mAb, in 200 μL 0.9% sterile saline for injection) *via* i.v. tail-vein injection. Approximately 5 minutes prior to recording PET images, mice were anesthetized by inhalation of 1% isoflurane (Baxter Healthcare, Deerfield, IL)/oxygen gas mixture and placed on the scanner bed. PET images were recorded at various time-points between 3–144 h post-injection. List-mode data were acquired for between 10 and 30 min. using a γ-ray energy window of 350–750 keV, and a coincidence timing window of 6 ns. For all static images, scan time was adjusted to ensure a minimum of 20 million coincident events were recorded. Data were sorted into 2-dimensional histograms by Fourier re-binning, and transverse images were reconstructed by filtered back-projection (FBP) into a 128×128×63 (0.72×0.72×1.3 mm) matrix. The reconstructed spatial resolution for ^{89}Zr was 1.9 mm full-width half maximum (FWHM) at the center of the field-of-view (FOV). The image data were normalized to correct for non-uniformity of response of the PET, dead-time count losses, positron branching ratio, and physical decay to the time of injection but no attenuation, scatter, or partial-volume averaging correction was applied. An empirically determined system calibration factor (in units of [mCi/mL]/[cps/voxel]) for mice was used to convert voxel count rates to activity concentrations. The resulting image data were then normalized to the administered activity to parameterize images in terms of %ID/g. Manually drawn 2-dimensional regions-of-interest (ROIs) or 3-dimensional volumes-of-interest

(VOIs) were used to determined the maximum and mean %ID/g (decay corrected to the time of injection) in various tissues.(29) Images were analyzed by using ASIPro VM™ software (Concorde Microsystems).

Full details of PET imaging of [^{89}Zr]Zr-chloride, [^{89}Zr]Zr-oxalate ([^{89}Zr(C_2O_4)$_4$]$^{4-}$) and [^{89}Zr]-Zr-DFO are presented in the supporting information.

Statistical analysis

Data were analysed by using the unpaired, two-tailed Student's *t*-test. Differences at the 95% confidence level (P<0.05) were considered to be statistically significant.

Results and discussion

Basic characterization of ^{89}Zr-species *in vivo*

Prior to commencing full studies on ^{89}Zr-radiolabeled mAbs, it is important to understand the *in vivo* behavior of various ^{89}Zr-labeled species including the starting reagents, and potential impurities or metabolites. Therefore, we examined the biodistribution of [^{89}Zr]Zr-chloride and [^{89}Zr]Zr-oxalate, and the complex, [^{89}Zr]Zr-DFO by using PET imaging (Figure 1). Maximum intensity projection (MIP) images of [^{89}Zr]Zr-chloride and [^{89}Zr]Zr-oxalate (300 μCi, 200 μL 0.9% sterile saline) were recorded at 24 h post-i.v. tail-vein injection in male, athymic, *nu/nu* mice.(24) [^{89}Zr]Zr-chloride was found to be sequestered in the liver with little excretion (Figure S1). In contrast, administration of [^{89}Zr]Zr-oxalate (most likely present as the thermodynamically stable species, [^{89}Zr(C_2O_4)$_4$]$^{4-}$) showed high accumulation of ^{89}Zr-radioactivity in bones, joints and potentially cartilage (Figure S2). Previous dynamic PET imaging studies on [^{89}Zr]Zr-DFO demonstrated that this complex is excreted rapidly within 20 min. *via* a renal pathway with a measured biological half-life ($t_{1/2.biol}$) of 305±6 s (Figures S3 and S4).

Density functional theory calculations

The complexation reaction between [^{89}Zr]Zr-chloride or [^{89}Zr]Zr-oxalate with the hexadentate, trihydroxamate chelate, desferrioxamine B (DFO) is shown in Scheme 1. In contrast to the more familiar coordination chemistry of radionuclides such as ^{64}Cu, ^{68}Ga, ^{111}In and $^{86/90}$Y, ^{89}Zr displays a number of distinct differences. In particular, the 4+ oxidation state imparts a strong preference for $^{89}Zr^{4+}$ ions to bind to highly electronegative (class a) hard donor atoms including oxygen, nitrogen and fluoride. Zirconium complexes have a high propensity towards hydrolysis in aqueous solution. In addition, the relatively large ionic radius of $^{89}Zr^{4+}$ allows the first coordination sphere to accommodate up to 8-donor atoms. In this respect, the ionic nature of most Zr^{4+} complexes and the higher coordination numbers means that the chemistry more closely resembles that of radio-lanthanides and radio-actinides such as ^{177}Lu and ^{225}Ac.

As a consequence of the complicated aqueous-phase chemistry, the nature of the most $^{89}Zr^{4+}$(aq.) species, including the [^{89}Zr]Zr-DFO complex is uncertain. Unfortunately, all attempts at crystallizing [^{89}Zr]Zr-DFO have been unsuccessful. Therefore, we conducted high level density functional theory (DFT) calculations to probe the structure, bonding and chemical/thermodynamic stability of [^{89}Zr]Zr-DFO with respect to expansion of the coordination sphere from 6- to 7- or 8-coordinate with the addition of one or two water molecules.

Structures of the octahedral complex [^{89}Zr(HDFO)]$^{2+}$ (**1**), the 7-coordinate complexes with *mono*-H_2O coordination in the axial and equatorial sites [^{89}Zr(HDFO)-ax-(H_2O)]$^{2+}$ (**2-ax**) and [^{89}Zr(HDFO)-eq-(H_2O)]$^{2+}$ (**2-eq**), and the 8-coordinate *bis*-H_2O complex

[^{89}Zr(HDFO)-*cis*-$(H_2O)_2$]$^{2+}$ (**3-*cis***) were fully optimized using DFT (Cartesian coordinates are given in the supporting information: Tables S1 – S5). Selected structural parameters for complexes **1** – **3** are presented in Table 1 and their relative energies and optimized structures are shown in the reaction coordinate diagram (Figures 2 and S5). The calculations reveal that expansion of the coordination sphere to either 7- or 8-coordinate by the addition of one or two water molecules is thermodynamically favorable. Interestingly, in the 7-coordinate species the axial and equatorial coordination sites, **2-ax** and **2-eq**, are energetically inequivalent. Axial coordination (**2-ax**) is thermodynamically more favorable than equatorial coordination (**2-eq**) by around −41 kJ mol^{-1}. The DFT calculations also suggest that the 8-coordinate complex with *cis*-coordination geometry with respect to the orientation of the H_2O molecules (**3-*cis***) is 95 kJ mol^{-1} more stable that the parent octahedral complex (**1**). Furthermore, complex **3-*cis*** is 14 kJ mol^{-1} more stable than the sum of the thermodynamic stabilization of achieved by complexes **2-ax** and **2-eq** (sum = −81 kJ mol^{-1}). This additional stability of complex **3-*cis*** arises due to structural relaxation from the cooperativity of two coordinated H_2O ligands which allows the *r*(Zr-OH_2(ax)) to decrease from 2.362 Å in complex **2-ax** to 2.33 Å in complex **3-*cis*** (Table 1). Natural bond order (NBO) charge analysis (Table S6) also supports the conclusion that thermodynamic stabilization of complex **3-*cis*** arises from increased electrostatic interaction between the Zr^{4+} ion and axial-H_2O ligand (ligand-to-metal charge transfer). NB: It should be noted that we expect the coordinated H_2O ligands to be kinetically labile and species **1** – **3** are likely in rapid equilibrium at physiological temperatures.

Previous studies have shown that although DTPA can be used for chelation and radiolabeling of mAbs with $^{89}Zr^{4+}$ ions, demetalation occurs *in vivo*, and although less than optimal, DFO remains the chelate of choice.(24,30,31) Experimental studies on ^{89}Zr-DFO-mAbs have reported high *in vivo* stability with respect to demetalation/ligand dissociation, and relatively low levels of radiotracer accumulation in background tissue.(32–37) These DFT studies suggest that the origin of the observed *in vivo* stability of ^{89}Zr-DFO-mAbs is a combination of the inherently high thermodynamic and kinetic stability of the [^{89}Zr]Zr-DFO complex due to very strong electrostatic interactions, coupled with the enhancement in thermodynamic stability induced by expansion of the first coordination sphere and geometry relaxation to give an 8-coordinate species. Indeed, in the case of [^{89}Zr]Zr-DFO, and in contrast to the more familiar Cu, Ga, In, and Y complexes, these studies indicate that the presence of water or, for example, coordinating anions such as chloride, actually increases the thermodynamic stability of the Zr complex.

Radiochemistry

J591 was functionalized with DFO by using bioconjugation methods modified from the pioneering work of Verel *et al*.(23) The conjugation and purification chemistry was found to proceed in moderate-to-high yield (65±5%) with high chemical purity (>95%). Radiolabeling of DFO-J591 with [^{89}Zr]Zr-oxalate was achieved at room temperature in slightly alkaline solutions (pH7.7–8.1) with crude radiochemical yields (>95%, *n*=6). Facile purification of ^{89}Zr-DFO-J591 from small-molecule radiolabeled impurities was achieved by using either size-exclusion chromatography or spin-column centrifugation. The final radiochemical yield of the purified ^{89}Zr-DFO-J591 was >77% and the product was formulated in 0.9% sterile saline with RCP >99% (*n*=6) and a specific-activity of 181.7±1.1 MBq/mg (4.91±0.03 mCi/mg) of mAb (Figures S6 and S7). The specific-activity obtained in these studies compares favorably with the previously reported specific-activities of other ^{89}Zr-radiolabeled mAbs.(32–39) Isotopic dilution assays revealed an average of 3.9±0.3 accessible chelates per mAb.

^{89}Zr-DFO-J591 immunoreactivity and stability studies *in vitro*

The immunoreactive fraction of the ^{89}Zr-DFO-J591 formulations was measured by specific *in vitro* cellular association assays using LNCaP (PSMA-positive) cells prior to each *in vivo* experiment (Figure S8).(26) In studies using [^{213}Bi]-labeled J591, McDevitt *et al*. reported that the LNCaP cell line has an estimated 180,000 PSMA molecules per cell.(11) However, in other studies using ^{111}In and ^{131}I-labeled mAbs (including J415, J533, J591 and 7E11), Smith-Jones *et al*. found higher PSMA copy numbers of between 600,000 – 800,000 sites/cell for viable LNCaP cells.(9) The average immunoreactive fraction of ^{89}Zr-DFO-J591 was found to be 0.95±0.03 (n=4). Control experiments (n=4) using the PC-3 (PSMA-negative) cell line showed no binding which further demonstrated the specificity of ^{89}Zr-DFO-J591 for PSMA expressing cells.

Incubation of ^{89}Zr-DFO-J591 in either 0.9% saline or 1% BSA for 7 days at 37°C revealed <2% decrease in RCP (*via* demetalation) with an observed ~17% decrease in the immunoreactive fraction for the 1% BSA experiment (0.78±0.03, Figure S9). Therefore, in the absence of specific proteolysis or reductive/oxidative metabolism, ^{89}Zr-DFO-J591 is expected to remain intact and immunoreactive *in vivo* on a time-scale suitable for immunoPET imaging.

Biodistribution studies

The ability of ^{89}Zr-DFO-J591 to target an extracellular epitope of the PSMA type II transmembrane glycoprotein receptor *in vivo* was initially assessed by conducting acute biodistribution studies in LNCaP tumor-bearing mice at 24, 48, 96 and 144 h post-i.v. administration (Tables 2 and S7, and Figure 3). The data reveal that high LNCaP tumor uptake was observed 24 h post-injection (34.4±3.2 %ID/g) with a steady increase through 48 h (38.0±6.2 %ID/g) and 96 h (40.4±4.8 %ID/g), and reaching 45.8±3.2 %ID/g at 144 h (P=0.01 between LNCaP uptake at 24 and 144 h). This high accumulation of ^{89}Zr-DFO-J591 is consistent with extraction of the activity from the blood pool (24 h: 21.8±2.8 %ID/g, 48 h: 4.4±1.9 %ID/g and 96 h: 1.4±0.8), rapid internalization of the J591-PSMA complex followed by sequestration of the ^{89}Zr-radioactivity inside the cell. In contrast, ^{89}Zr-DFO-J591 uptake in the PC-3 (PSMA negative) tumors at 48 h (15.6±2.1 %ID/g, P=0.0025) and 96 h (24.0±2.6 %ID/g, P=0.0017) showed statistically significant decrease in ^{89}Zr-accumulation compared with uptake in PSMA-positive tumors. In mice bearing PC-3 tumors, the ^{89}Zr-DFO-J591 activity in the blood remained 4-fold higher at 48 h (19.0±1.1 %ID/g, P=0.001) and 10-fold at 96 h (13.0±1.8 %ID/g, P<0.05) compared with the corresponding LNCaP mice (48 h: 4.4±1.9 %ID/g and 96 h: 1.4±0.8 %ID/g).

Competitive inhibition (“blocking”) studies using low specific-activity formulations (60-fold decrease: 3.04 MBq/mg, [0.082 mCi/mg]) revealed only 10.3±0.8 %ID/g tumor uptake at 48 h post-injection; an approximate 4-fold decrease (P<0.002) *versus* high specific-activity formulations (Table 2 and Figure 3). Furthermore, in the low specific-activity experiments, ^{89}Zr-DFO-J591 activity in the blood remained high (2–3 fold higher at 48 h: 10.7±0.4 %ID/g, P=0.026) but ^{89}Zr-accumulation in the liver showed a statistically significant decrease from 17.7±1.6 %ID/g to 5.1±0.4 %ID/g (P<0.004). This decreased liver uptake on increasing the mass of administered mAb is fully consistent with the reported decreased liver toxicity observed in Phase I dose escalation trials. The competitive inhibition experiments concur with the *in vitro* data (*vide supra*) and further demonstrate the specificity of ^{89}Zr-DFO-J591 for the PSMA antigen *in vivo*.

Interestingly, in the LNCaP tumor-bearing mice ^{89}Zr uptake in the bone was relatively high and increased between 24 to 96 h (24 h: 4.0±0.8 %ID/g, 48 h: 8.2±1.2 %ID/g and 96 h: 8.7±1.5), before decreasing slightly to 7.4±1.3 %ID/g at 144 h. In contrast, bone

accumulation of ^{89}Zr activity in the PC-3 tumor-bearing mice was reduced in magnitude by approximately 45% at 48 and 96 h (4.3±0.6 %ID/g and 5.1±0.5 %ID/g, respectively). The degree of bone uptake is consistent with previously reported studies using various other ^{89}Zr-labeled mAbs including ^{89}Zr-DFO-trastuzumab (37,39) for imaging HER2/*neu* expression and ^{89}Zr-DFO-bevacizumab for imaging vascular endothelial growth factor (VEGF).(40) The nature of the radioactive species accumulating in the bone remains uncertain but it is plausible that slow intratumoral metabolism and subsequent recirculation of ^{89}Zr-labeled metabolites may occur. Full metabolic studies are beyond the scope of the current study and will be the subject of further investigations. However, it is worth noting that in a recent clinical trial investigating the radiation dosimetry of ^{89}Zr-DFO-U36 (a chimeric monoclonal antibody directed against CD44v6) in 20 patients with head and neck squamous cell carcinoma (HNSCC), the liver was identified as the dose limiting organ. (34,38)

ImmunoPET imaging with ^{89}Zr-DFO-J591

Temporal immunoPET images of ^{89}Zr-DFO-J591 (10.9–11.3 MBq, [295–305 μCi], 60–62 μg of mAb, in 200 μL 0.9% sterile saline) recorded in LNCaP and PC-3 tumor-bearing mice between 3 to 144 h are presented in Figure 4. Time-activity curves (TACs) generated from the immunoPET images showing the mean %ID/g radiotracer uptake in various tissues including the heart/blood pool, liver and muscle in mice bearing LNCaP (*n*=3) or PC-3 (*n*=3) are given in Figure 5. Radiotracer uptake in LNCaP tumors was observed in <24 h post-injection of ^{89}Zr-DFO-J591 and high tumor-to-muscle (T/M) ratios (calculated by using the mean %ID/g values derived from volume-of-interest [VOI]) analysis of the immunoPET images) were observed. At 48 h post-injection the immunoPET measured mean and maximum %ID/g for radiotracer uptake in LNCaP tumor-bearing mice were found to be 21.9±0.6 and 38.2±4.9 %ID/g, respectively, with a mean T/M ratio of 15.85 (Table S8). By 120 and 144 h, the mean T/M ratio in LNCaP tumors increased to 22.49 and 25.89, respectively. In contrast, low ^{89}Zr-DFO-J591 accumulation in PSMA-negative PC-3 tumors (mean T/M ratios of 3.48, 4.36 and 4.19 at 48, 120 and 144 h, respectively) was found to occur. Uptake in these PSMA-negative tumors is in accordance with the “enhanced permeation and retention” (EPR) mechanism (Table S9 and Figures S10 – S12).

These data demonstrate that ^{89}Zr-DFO-J591 immunoPET imaging provides very high tumor-to-background tissue (T/B) ratios and that this high uptake is specific for the presence of PSMA expression in tissue. Overall, the novel radiotracer ^{89}Zr-DFO-J591 represents a promising candidate for translation to the clinic as an immunoPET agent for non-invasive delineation of PSMA-positive primary and metastatic prostate cancers *in vivo*.

Summary and Conclusions

Basic characterization of the *in vivo* behavior of several important ^{89}Zr-labeled species, including the starting reagents, [^{89}Zr]Zr-chloride and [^{89}Zr]Zr-oxalate, and the key complex [^{89}Zr]Zr-DFO are reported. Using PET imaging, the nature of the aqueous phase ^{89}Zr species was shown to have a dramatic effect on the *in vivo* biodistribution with [^{89}Zr]Zr-chloride and [^{89}Zr]Zr-oxalate sequestering for over 24 h in the liver and bones, respectively. In contrast, [^{89}Zr]Zr-DFO is first pass excreted through the kidneys and accumulates in the bladder with a biological half-life of 305±6 s.

The nature of the [^{89}Zr]Zr-DFO complex and its thermodynamic stability with respect to expansion of the coordination environment from 6- to 7- or 8-coordinate through the addition of one or two water ligands has been investigated using high level DFT calculations. The computational studies suggest that formation of an 8-coordinate complex with two labile water ligands is thermodynamically favorable and in this respect, aqueous

environments are expected to actively increase the inherent thermodynamic stability of ^{89}Zr-DFO-conjugated radiotracers.

^{89}Zr-DFO-J591 has been prepared with high radiochemical purity (>99%) and specific-activity (of 181.7±1.1 MBq/mg). *In vitro* stability studies demonstrated that functionalization of J591 with 3.9±0.3 accessible DFO chelates per mAb, and subsequent radiolabeling does not compromise the immunoreactivity, and radiolabeled immunoconjugate remains active for up to 7 days at 37°C. Biodistribution and immunoPET experiments indicated that ^{89}Zr-DFO-J591 shows high potential as a radiotracer for specific, non-invasive delineation of PSMA positive prostate cancers *in vivo*. Work towards the clinical translation of ^{89}Zr-DFO-J591 and other ^{89}Zr-labeled mAbs is underway.

Supplementary Material

Refer to Web version on PubMed Central for supplementary material.

Acknowledgments

We thank Drs. NagaVaraKishore Pillarsetty and Pat Zanzonico for informative discussions, Valerie M. Longo for assistance with the biodistribution experiments, Thomas Ku for advice with *in vitro* experiments and Bradley Beattie for assistance with the PET imaging. We thank Prof. Jennifer C. Green (Department of Chemistry, University of Oxford, United Kingdom) for access to computational facilities. We also thank the staff of the Radiochemistry/Cyclotron Core at MSKCC.

Grant Support: Funded in part by the Geoffrey Beene Cancer Research Center of Memorial Sloan-Kettering Cancer Center (JSL), the Office of Science (BER) - U. S. Department of Energy (Award DE-SC0002456; JSL), the Ludwig Center for Cancer Immunotherapy of the Sloan-Kettering Institute (SML, PSJ) and the Starr Cancer Consortium (SML, JSL and PSJ). Technical services provided by the MSKCC Small-Animal Imaging Core Facility were supported in part by NIH grants R24 CA83084 and P30 CA08748.

References

1. Apolo AB, Pandit-Taskar N, Morris MJ. Novel tracers and their development for the imaging of metastatic prostate cancer. J Nucl Med 2008;49(12):2031–2041. [PubMed: 18997047]
2. Olson WC, Heston WDW, Rajasekaran AK. Clinical trials of cancer therapies targeting prostate-specific membrane antigen. Reviews on Recent Clinical Trials 2007;2:182–190. [PubMed: 18474004]
3. Jhanwar YS, Divgi C. Current status of therapy of solid tumors. J Nucl Med 2005;46(1_suppl): 141S–150S. [PubMed: 15653662]
4. Sokoloff RL, Norton KC, Gasior CL, Marker KM, Grauer LS. A dual-monoclonal sandwich assay for prostate-specific membrane antigen: Levels in tissues, seminal fluid and urine. The Prostate 2000;43(2):150–157. [PubMed: 10754531]
5. Manyak MJ. Indium-111 capromab pendetide in the management of recurrent prostate cancer. Expert Rev Anticancer Ther 2008;8(2):175–181. [PubMed: 18279057]
6. Morris MJ, Pandit-Taskar N, Divgi CR, et al. Phase I evaluation of J591 as a vascular targeting agent in progressive solid tumors. Clin Cancer Res 2007;13(9):2707–2713. [PubMed: 17473203]
7. Liu H, Moy P, Kim S, et al. Monoclonal antibodies to the extracellular domain of prostate-specific membrane antigen also react with tumor endothelium. Cancer Res 1997;57:3629–3634. [PubMed: 9288760]
8. Liu H, Rajasekaran AK, Moy P, et al. Constitutive and antibody-induced internalization of prostate-specific membrane antigen. Cancer Res 1997;58:4055–4060. [PubMed: 9751609]
9. Smith-Jones PM, Vallabahajosula S, Goldsmith SJ, et al. In vitro characterization of radiolabeled monoclonal antibodies specific for the extracellular domain of prostate-specific membrane antigen. Cancer Res 2000;6(18):5237–5243. [PubMed: 11016653]
10. Smith-Jones PM, Vallabhajosula S, Navarro V, Bastidas D, Goldsmith SJ, Bander NH. Radiolabeled monoclonal antibodies specific to the extracellular domain of prostate-specific

membrane antigen: preclinical studies in nude mice bearing LNCaP human prostate tumor. J Nucl Med 2003;44(4):610–617. [PubMed: 12679407]

11. McDevitt MR, Barendswaard E, Ma D, et al. An {{alpha}}-particle emitting antibody ([^{213}Bi]J591) for radioimmunotherapy of prostate cancer. Cancer Res 2000;60(21):6095–6100. [PubMed: 11085533]
12. Vallabahajosula S, Smith-Jones PM, Navarro V, Goldsmith SJ, Bander NH. Radioimmunotherapy of prostate cancer in human xenografts using monoclonal antibodies specific to prostate specific membrane antigen (PSMA): studies in nude mice. The Prostate 2004;58:145–155. [PubMed: 14716739]
13. Vallabhajosula S, Kuji I, Hamacher KA, et al. Pharmacokinetics and biodistribution of ^{111}In- and ^{177}Lu-labeled J591 antibody specific for prostate-specific membrane antigen: prediction of ^{90}Y-J591 radiation dosimetry based on ^{111}In or ^{177}Lu? J Nucl Med 2005;46(4):634–641. [PubMed: 15809486]
14. Bander NH, Trabulsi EJ, Kostakoglu L, et al. Targeting metastatic prostate cancer with radiolabeled monoclonal antibody J591 to the extracellular domain of prostate specific membrane antigen. J Urology 2003;170:1717–1721.
15. Vallabhajosula S, Goldsmith SJ, Hamacher KA, et al. Prediction of myelotoxicity based on bone marrow radiation-absorbed dose: radioimmunotherapy studies using ^{90}Y- and ^{177}Lu-labeled J591 antibodies specific for prostate-specific membrane antigen. J Nucl Med 2005;46(5):850–858. [PubMed: 15872360]
16. Vallabhajosula S, Goldsmith SJ, Kostakoglu L, Milowsky M, Nanus DM, Bander NH. Radioimmunotherapy of prostate cancer using ^{90}Y- and ^{177}Lu-labeled J591 monoclonal antibodies: effect of multiple treatments on myelotoxicity. Clin Cancer Res 2005;11(19Suppl): 7195s–7200s. [PubMed: 16203821]
17. Bander NH, Milowsky MI, Nanus DM, Kostakoglu L, Vallabhajosula S, Goldsmith SJ. Phase I trial of ^{177}Lu-labeled J591, a monoclonal antibody to prostate-specific membrane antigen, in patients with androgen-independent prostate cancer. J Clin Oncology 2005;23(21):4591–4601.
18. Milowsky MI, Nanus DM, Kostakoglu L, et al. Vascular targeted therapy with anti-prostate-specific membrane antigen monoclonal antibody J591 in advenced solid tumors. J Clin Oncology 2007;25(5):540–547.
19. Pandit-Taskar N, O'Donoghue JA, Morris MJ, et al. Antibody mass escalation study in patients with castration-resistant prostate cancer using ^{111}In-J591: lesion detectability and dosimetric projections for ^{90}Y radioimmunotherapy. J Nucl Med 2008;49(7):1066–1074. [PubMed: 18552139]
20. McDevitt MR, Ma D, Lai LT, et al. Tumor therapy with targeted atomic nanogenerators. Science 2001;294(5546):1537–1540. [PubMed: 11711678]
21. Zanzonico P. Routine quality control of clinical nuclear medicine instrumentation: a brief review. J Nucl Med 2009;49(7):1114–1131. [PubMed: 18587088]
22. Gaussian 03 RC. Frisch, MJ.; Trucks, GW.; Schlegel, HB.; Scuseria, GE.; Robb, MA.; Cheeseman, JR.; Montgomery, JA., Jr; Vreven, T.; Kudin, KN.; Burant, JC.; Millam, JM.; Iyengar, SS.; Tomasi, J.; Barone, V.; Mennucci, B.; Cossi, M.; Scalmani, G.; Rega, N.; Petersson, GA.; Nakatsuji, H.; Hada, M.; Ehara, M.; Toyota, K.; Fukuda, R.; Hasegawa, J.; Ishida, M.; Nakajima, T.; Honda, Y.; Kitao, O.; Nakai, H.; Klene, M.; Li, X.; Knox, JE.; Hratchian, HP.; Cross, JB.; Bakken, V.; Adamo, C.; Jaramillo, J.; Gomperts, R.; Stratmann, RE.; Yazyev, O.; Austin, AJ.; Cammi, R.; Pomelli, C.; Ochterski, JW.; Ayala, PY.; Morokuma, K.; Voth, GA.; Salvador, P.; Dannenberg, JJ.; Zakrzewski, VG.; Dapprich, S.; Daniels, AD.; Strain, MC.; Farkas, O.; Malick, DK.; Rabuck, AD.; Raghavachari, K.; Foresman, JB.; Ortiz, JV.; Cui, Q.; Baboul, AG.; Clifford, S.; Cioslowski, J.; Stefanov, BB.; Liu, G.; Liashenko, A.; Piskorz, P.; Komaromi, I.; Martin, RL.; Fox, DJ.; Keith, T.; Al-Laham, MA.; Peng, CY.; Nanayakkara, A.; Challacombe, M.; Gill, PMW.; Johnson, B.; Chen, W.; Wong, MW.; Gonzalez, C.; Pople, JA. Wallingford CT: Gaussian, Inc.; 2004.
23. Verel I, Visser GWM, Boellaard R, Stigter-van Walsum M, Snow GB, van Dongen GAMS. ^{89}Zr immuno-PET: Comprehensive procedures for the production of ^{89}Zr-labeled monoclonal antibodies. J Nucl Med 2003;44:1271–1281. [PubMed: 12902418]

24. Holland JP, Sheh Y, Lewis JS. Standardized methods for the production of high specific-activity zirconium-89. Nucl Med Biol 2009;36(7):729–739. [PubMed: 19720285]
25. Anderson CJ, Schwarz SW, Connett JM, et al. Preparation, biodistribution and dosimetry of copper-64-labeled anti-colorectal carcinoma monoclonal antibody fragments 1A3-F(ab')2. J Nucl Med 1995;36(5):850–858. [PubMed: 7738663]
26. Lindmo T, Boven E, Cuttitta F, Fedorko J, Bunn PA Jr. Determination of the immunoreactive fraction of radiolabeled monoclonal antibodies by linear extrapolation to binding at infinite antigen excess. J Immunological Methods 1984;72(1):77–89.
27. Smith-Jones PM, Solit D, Afroze F, Rosen N, Larson SM. Early tumor response to Hsp90 therapy using HER2 PET: Comparison with ^{18}F-FDG PET. J Nucl Med 2006;47:793–796. [PubMed: 16644749]
28. Kim JS, Lee JS, Im KC, et al. Performance measurement of the microPET Focus 120 scanner. J Nucl Med 2007;48(9):1527–1535. [PubMed: 17704248]
29. Tseng J-C, Zanzonico PB, Levin B, Finn R, Larson SM, Meruelo D. Tumor-specific in vivo transfection with HSV-1 thymidine kinase gene using a sindbis viral vector as a basis for prodrug ganciclovir activation and PET. J Nucl Med 2006;47:1136–1143. [PubMed: 16818948]
30. Meijs WE, Herscheid JDM, Haisma HJ, Pinedo HM. Evaluation of desferal as a bifunctional chelating agent for labeling antibodies with Zr-89. Appl Radiat Isot 1992;43(12):1443–1447.
31. Meijs WE, Haisma HJ, Klok RP, et al. Zirconium-labeled monoclonal antibodies and their distribution in tumor-bearing nude mice. J Nucl Med 1997;38:112–118. [PubMed: 8998164]
32. Verel I, Visser GWM, Boellaard R, et al. Quantitative ^{89}Zr immuno-PET for in vivo scouting of ^{90}Y-labeled monoclonal antibodies in Xenograft-bearing nude mice. J Nucl Med 2003;44:1663–1670. [PubMed: 14530484]
33. Perk LR, Visser OJ, Stigter-van Walsum M, et al. Preparation and evaluation of ^{89}Zr-Zevalin for monitoring of ^{90}Y-Zevalin biodistribution with positron emission tomography. Eur J Nucl Med Mol Imaging 2006;33(11):1337–1345. [PubMed: 16832633]
34. Börjesson PKE, Jauw YWS, Boellaard R, et al. Performance of immuno-Positron Emission Tomography with Zirconium-89-labeled chimeric monoclonal antibody U36 in the detection of lymph node metastases in head and neck cancer patients. Clin Cancer Res 2006;12(7):2133–2140. [PubMed: 16609026]
35. Perk LR, Stigter-van Walsum M, Visser GWM, et al. Quantitative PET imaging of Met-expressing human cancer xenografts with ^{89}Zr-labelled monoclonal antibody DN30. Eur J Nucl Med Mol Imaging 2008;35(10):1857–1867. [PubMed: 18491091]
36. Aerts HJWL, Dubois L, Perk L, et al. Disparity between in vivo EGFR expression and 89Zr-labeled cetuximab uptake assessed with PET. J Nucl Med 2009;50(1):123–131. [PubMed: 19091906]
37. Dijkers ECF, Kosterink JGW, Rademaker AP, et al. Development and characterization of clinical-grade ^{89}Zr-trastuzumab for HER2/neu immunoPET imaging. J Nucl Med 2009;50(6):974–981. [PubMed: 19443585]
38. Borjesson PKE, Jauw YWS, de Bree R, et al. Radiation dosimetry of ^{89}Zr-labeled chimeric monoclonal antibody U36 as used for immuno-PET in head and neck cancer patients. J Nucl Med 2009;50(11):1828–1836. [PubMed: 19837762]
39. Holland JP, Caldas-Lopes E, Divilov V, et al. Measuring the pharmacokinetic effects of a novel Hsp90 inhibitor on HER2/*neu* expression in mice using ^{89}Zr-DFO-trastuzumab. PLoS ONE 2010;5(1):e8859. [PubMed: 20111600]
40. Nagengast WB, de Vries EG, Hospers GA, et al. In vivo VEGF imaging with radiolabeled bevacizumab in a human ovarian tumor xenograft. J Nucl Med 2007;48(8):1313–1319. [PubMed: 17631557]

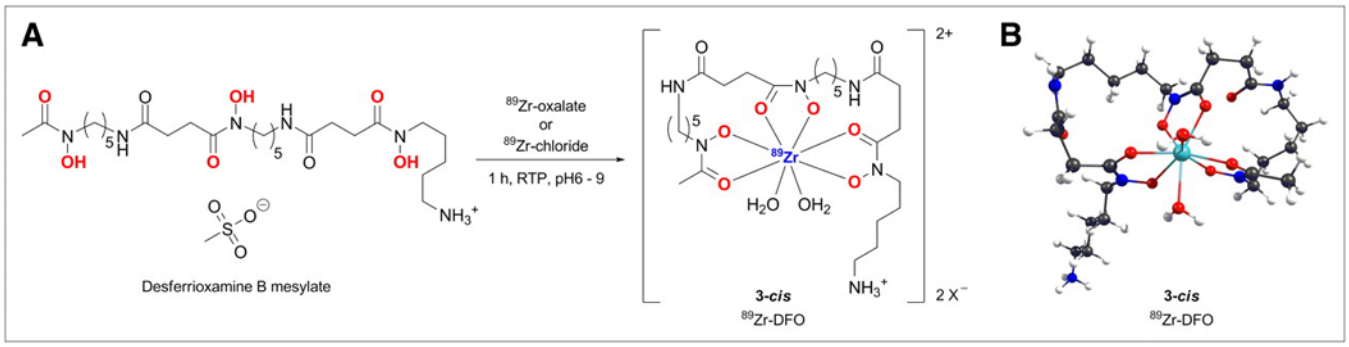

Figure 1.

(A) Complexation reaction between $[^{89}Zr(C_2O_4)_4]^{4-}$ and DFO. (B) DFT-optimized structure of 8-coordinate complex $[^{89}Zr(HDFO)\text{-}cis\text{-}(H_2O)_2]^{2+}$ (**3-*cis***).

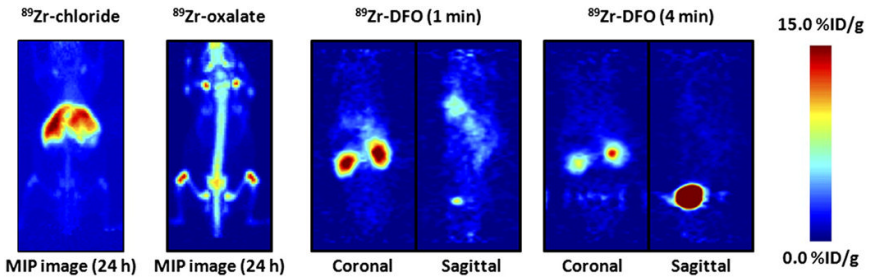

Figure 2.

PET images showing maximum intensity projection of ^{89}Zr-chloride and ^{89}Zr-oxalate at 24 h after intravenous administration and dynamic PET images of ^{89}Zr-DFO at 1 and 4 min after injection. For maximum-intensity-projection images, upper and lower intensity thresholds were set at 100% and 0%, respectively. Further details are presented in Supplemental Figures 3–6. MIP = maximum intensity projection.

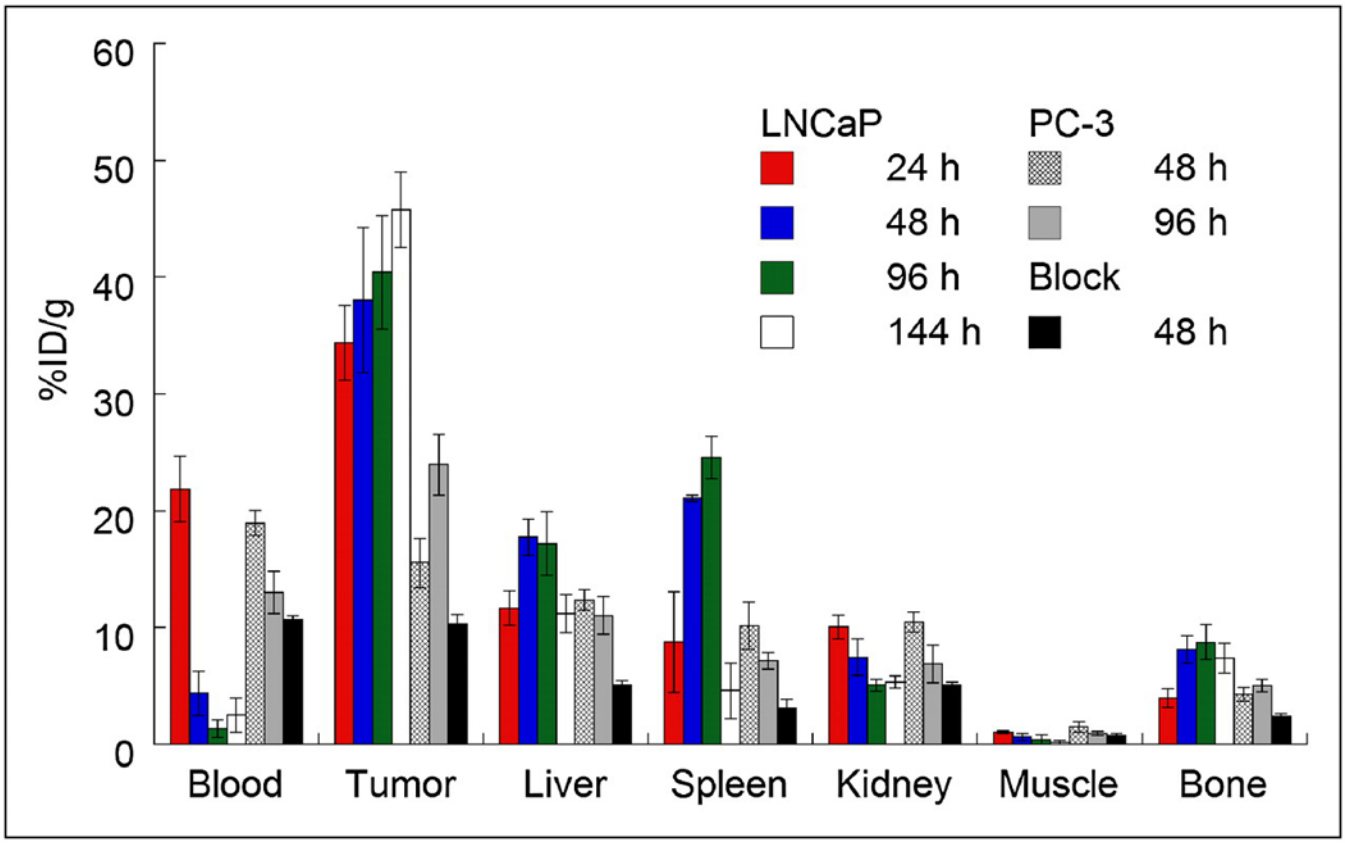

Figure 3.

Bar chart showing selected tissue biodistribution data (%ID/g) for uptake of either high- (181.7 ± 1.1 MBq/mg [4.91 ± 0.03 mCi/mg]; 3–4 μg of mAb per mouse) or low-specific-activity (60-fold decrease, 3.04 MBq/mg [0.082 mCi/mg]; 300 μg of mAb per mouse) formulations of ^{89}Zr-DFO-J591 (0.55–0.74 MBq [15–20 μCi], in 200 μL of sterile saline for injection) in male athymic nu/nu mice bearing subcutaneous LNCaP (PSMA-positive) or PC-3 (PSMA-negative) tumors.

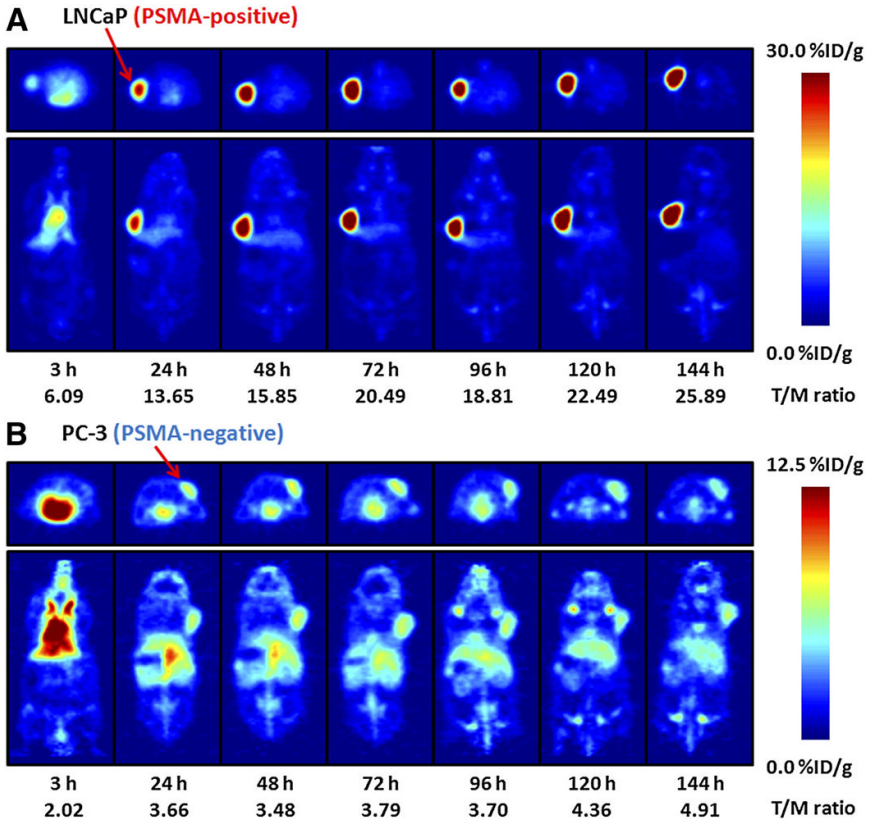

Figure 4.

Temporal immunoPET images of ^{89}Zr-DFO-J591 (10.9–11.3 MBq [295–305 μCi], 60–62 μg of mAb, in 200 μL of sterile saline) recorded in LNCaP tumor–bearing (PSMA-positive, left shoulder) (A) and PC-3 tumor–bearing (PSMA-negative, right shoulder) (B) mice between 3 and 144 h after injection. Transverse and coronal planar images intersect center of tumors, and mean tumor-to-muscle ratios derived from volume-of-interest analysis of immunoPET images are given. Upper thresholds of immunoPET have been adjusted for visual clarity, as indicated by scale bars.

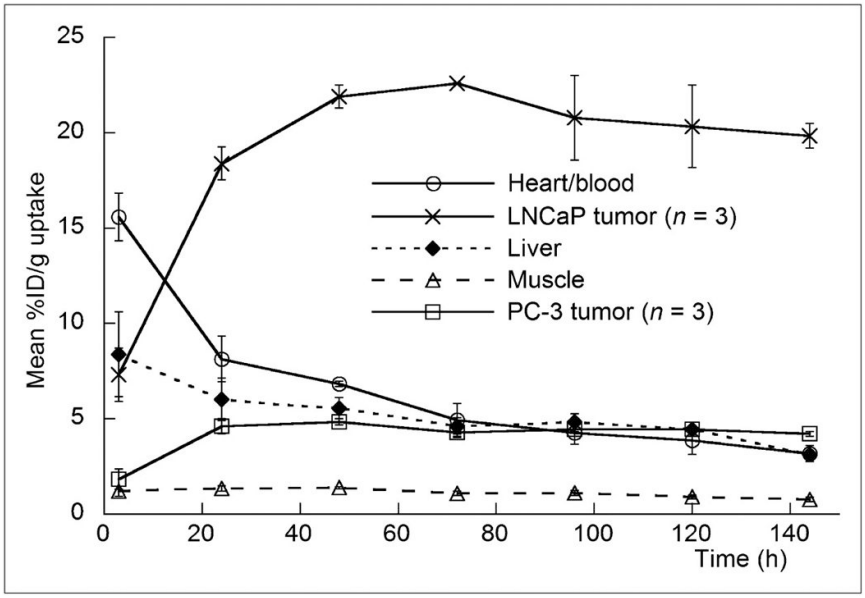

Figure 5.

Time–activity curves derived by volume-of-interest analysis of immunoPET images showing mean %ID/g tissue uptake vs. time/h for ^{89}Zr-DFO-J591 radiotracer accumulation in mice bearing subcutaneous LNCaP (PSMA-positive) or PC-3 (PSMA-negative) tumors. Complete time–activity curve data for ^{89}Zr-DFO-J591 immunoPET imaging is given in supplemental materials (Supplemental Tables 9 and 10; Supplemental Figs. 11–13).

TABLE 1

Biodistribution Data of ^{89}Zr-DFO-J591, Administered Intravenously to Mice Bearing Subcutaneous LNCaP Tumors

Organ	24 h (*n* = 4)	48 h (*n* = 5)	96 h (*n* = 5)	144 h (*n* = 4)	Block (300 μg of mAb) at 48 h (*n* = 4)
Blood	21.8 ± 2.8	4.4 ± 1.9	1.4 ± 0.8	2.6 ± 1.5	10.7 ± 0.4
Tumor	34.4 ± 3.2	38.0 ± 6.2	40.4 ± 4.8	45.8 ± 3.2	10.3 ± 0.8
Heart	7.4 ± 2.2	4.0 ± 1.3	1.7 ± 0.6	1.4 ± 0.5	3.8 ± 0.7
Lung	11.7 ± 1.9	5.7 ± 3.1	2.2 ± 0.9	2.5 ± 0.9	5.7 ± 0.3
Liver	11.7 ± 1.5	17.7 ± 1.6	17.2 ± 2.7	11.2 ± 1.6	5.1 ± 0.4
Spleen	8.8 ± 4.3	21.1 ± 0.3	24.6 ± 1.8	4.6 ± 2.4	3.1 ± 0.7
Kidney	10.1 ± 1.0	7.5 ± 1.5	5.1 ± 0.5	5.3 ± 0.5	5.1 ± 0.2
Muscle	1.1 ± 0.1	0.6 ± 0.3	0.4 ± 0.4	0.2 ± 0.2	0.8 ± 0.2
Bone	4.0 ± 0.8	8.2 ± 1.2	8.7 ± 1.5	7.4 ± 1.3	2.4 ± 0.3
Tumor/blood	1.6 ± 0.2	8.7 ± 4.1	29.7 ± 17.1	18.0 ± 10.5	1.0 ± 0.1
Tumor/heart	4.7 ± 1.5	9.6 ± 3.5	23.4 ± 9.0	31.9 ± 10.7	2.7 ± 0.5
Tumor/lung	2.9 ± 0.5	6.7 ± 3.7	18.4 ± 7.7	18.5 ± 6.8	1.8 ± 0.2
Tumor/liver	2.9 ± 0.5	2.1 ± 0.4	2.3 ± 0.5	4.1 ± 0.7	2.0 ± 0.2
Tumor/spleen	3.9 ± 1.9	1.8 ± 0.3	1.6 ± 0.2	9.9 ± 5.2	3.3 ± 0.8
Tumor/kidney	3.4 ± 0.5	5.1 ± 1.3	7.9 ± 1.2	8.6 ± 1.1	2.0 ± 0.2
Tumor/muscle	32.4 ± 4.6	59.2 ± 28.8	95.9 ± 95.3	306.4 ± 432.2	13.3 ± 3.1
Tumor/bone	8.7 ± 1.9	4.7 ± 1.0	4.6 ± 1.0	6.2 ± 1.2	4.3 ± 0.6

Complete biodistribution data are presented in Supplemental Table 7. Data are expressed as mean % ID/g ± SD. Errors for tumor-to-tissue ratios are calculated as geometric mean of SD. LNCaP tumors: 3–4 μg mAb; PSMA-positive, 50–250 mm^3.

TABLE 2

Biodistribution Data of ^{89}Zr-DFO-J591, Administered Intravenously to Mice Bearing Subcutaneous PC-3 Tumors (3–4 μg of mAb)

Organ	48 h (*n* = 4)	96 h (*n* = 3)
Blood	19.0 ± 1.1	13.0 ± 1.8
Tumor	15.6 ± 2.1	24.0 ± 2.6
Heart	6.8 ± 0.1	4.3 ± 0.9
Lung	12.6 ± 1.9	7.0 ± 2.3
Liver	12.4 ± 0.9	11.0 ± 1.6
Spleen	10.2 ± 2.0	7.2 ± 0.7
Kidney	10.5 ± 0.9	6.9 ± 1.6
Muscle	1.5 ± 0.4	0.9 ± 0.2
Bone	4.3 ± 0.6	5.1 ± 0.5
Tumor/blood	0.8 ± 0.1	1.8 ± 0.3
Tumor/heart	2.3 ± 0.3	5.6 ± 1.4
Tumor/lung	1.2 ± 0.3	3.4 ± 1.2
Tumor/liver	1.3 ± 0.2	2.2 ± 0.4
Tumor/spleen	1.5 ± 0.4	3.4 ± 0.5
Tumor/kidney	1.5 ± 0.2	3.5 ± 0.9
Tumor/muscle	10.4 ± 3.3	25.4 ± 5.8
Tumor/bone	3.6 ± 0.7	4.7 ± 0.7

Complete biodistribution data are presented in Supplemental Table 7. Data are expressed as mean %ID/g ± SD. Errors for tumor-to-tissue ratios are calculated as geometric mean of SD. PC-3 tumors: PSMA-negative, 70–90 mm^3.